Ultra-broadband and Wide-angle Metamaterial Absorber with Carbon Black/Carbonyl Iron Composites Fabricated by Direct-Ink-Write 3D Printing

*Zhe Zhang [1], Fei Wang [1], Jiliang Zhang [1], Peifeng Li [2], Kaiyong Jiang [1]**

1 Fujian Key Laboratory of Special Energy Manufacturing,
Xiamen Key Laboratory of Digital Vision Measurement,
Huaqiao University,
Xiamen 361021, P.R.China
E-mail: jiangky@hqu.edu.cn

2 James Watt School of Engineering,
University of Glasgow, Glasgow, G12 8QQ
United Kingdom

Keywords: ultra-broadband, carbon black/carbonyl iron composites, asymmetric woodpile, metamaterials, microwave absorption

This study proposes the fabrication of an asymmetric woodpile metamaterial absorber using direct-ink-writing 3D printing technology. The prepared inks are compounded using two loss fillers: carbon black and carbonyl iron powder. The synergistic effect enhances the electromagnetic loss performance and the synergistic mechanism is analyzed. The designed asymmetric woodpile absorber has a wider bandwidth than a simple tetragonal woodpile, and the advantage presented by the asymmetric woodpile arrangement overcomes the local impedance mismatch. A simulation is then performed, which demonstrates that the designed asymmetric woodpile metamaterial with a thickness of 8.6 mm can achieve a -10 dB absorbing bandwidth in the frequency range of 3.9 GHz to 18 GHz, and the maximum reflection loss reaches up to -39 dB. Additionally, the absorber exhibits excellent angular performance and the absorption bandwidth of the transverse electric polarization or transverse magnetic polarization waves can reach more than 10 GHz with incident angles from 0 ° to 50 °. Furthermore,

the manufacturing process of the absorber is simple, efficient, and inexpensive, which presents considerable potential for its widespread implementation in practical engineering applications.

1.Introduction

Microwave absorbers are a type of functional material which can significantly attenuate the energy of incident microwaves with minimal reflection.[1;2] Microwave absorbers with a wider effective absorption bandwidth (EAB) and better angular performance can adapt to more complex microwave working environments with a more effective protection ability for targets.[3;4] Extensive research has been conducted on the modification of dielectric loss or magnetic loss fillers to widen the EAB. Some studies have demonstrated that the mixing of the two types of loss fillers can regulate the electromagnetic parameters of the composites.[5;9] This helps in improving the impedance matching performance and in widening the range of the EAB; however, it still cannot fully satisfy the requirements of ultra-broadband and wide-angle microwave absorption.

Electromagnetic metamaterials are special periodic structures which are designed and fabricated artificially; their periodic unit cell is much smaller than the wavelength of EM waves.[10;12] Their electromagnetic properties primarily depend on the unit structure of the metamaterials and not entirely on the intrinsic properties of the material itself. Some recent studies have reported that the EAB can be effectively widened by using electromagnetic metamaterials. Zhuang et al.[13] proposed a magnetic metamaterial structure based on an FeCo soft magnetic composite with a droplet shape as the primary resonant element; its bandwidth reached 6 GHz. The droplet-shaped units formed by the metal mold were periodically arranged and pasted onto the FR-4 substrate. However, the fabrication process is relatively complicated and it is difficult to ensure the forming accuracy. Pang et al.[14] proposed a double-corrugated metamaterial which requires standard mechanical milling of the designed double-corrugated structure on a commercial copper/FR4 multilayered printed circuit board (PCB). This metamaterial presents an absorbance of more than 80% in the frequency range of 7.22 GHz-18 GHz. The conventional fabrication processes used to fabricate complex structures are cumbersome, which limits the research and development of metamaterial microwave absorbers.

Three-dimensional (3D) printing technology has been demonstrated to be more effective when compared to the conventional 3D metamaterial manufacturing method and can overcome the processing difficulties presented by the complexity of the metamaterial absorbing structure. Its high flexibility compensates for the design limitation, which typically results in additional microwave loss through the structure and further widens the EAB. [15;17] Current studies are primarily focused on Fusion Deposition Modeling (FDM), Digital Light Processing (DLP), and Stereo lithography Apparatus (SLA); the structures prepared by these processes exhibit a wide EAB.[18;29] However, a few studies have been conducted on direct-ink-writing (DIW) 3D printing, which involves printing large-sized geopolymer-based composite microwave absorption structures.[30] Contrary to the thermoplastic materials used in FDM, the DIW process uses thermosetting or ceramic materials as the matrix, which presents strong mechanical properties and thermal stability. Additionally, the DIW process can compound multiple absorbing fillers with higher additive amounts than the DLP or SLA, which helps in achieving stronger microwave absorption performance.

In this study, we used unsaturated polyester (UP) and epoxy resin (EP) as the matrix, carbon black (CB) as the dielectric loss-absorbing filler, carbonyl iron powder (CIP) as the magnetic loss-absorbing filler, and mixed and prepared multi-loss composite inks. Subsequently, the electromagnetic properties of the CB/CIP composites were measured and analyzed. A gradient index (GRIN) asymmetric woodpile metamaterial microwave absorber was designed and fabricated using DIW 3D printing technology. The arrangement of the woodpiles can be optimized to alleviate the impedance mismatch phenomenon in the local area. The low-frequency microwave can propagate from the surface to the bottom layer of the structure and be absorbed, resulting in a slight widening of the EAB. Simulations and experiments were then performed, which demonstrate that the designed absorber can achieve an ultra-broadband absorption of 3.9 GHz-18 GHz at a thickness of 8.6 mm, and exhibits good wide-angle microwave absorption ability. The method used for the fabrication of broadband wide-angle metamaterial absorbing structures was simple and inexpensive, and presents considerable potential for various engineering applications.

2.Experimental

2.1 Materials

The epoxy resin (E51) was provided by Guangzhou Suixin Chemical Co., Ltd.; epoxy resin curing agent (HAA 1021) was provided by LOHO High-tech Materials (Shanghai) Co., Ltd.; 196 unsaturated polyester and its curing agent (MEKP) was provided by

Dongguan Huaxun New Materials Technology Co., Ltd.; carbon black (CB, diameter: 30–40 nm) was provided by Tianjin Zhengyuan Technology Co., Ltd.; carbonyl iron powder (CIP, diameter:3-5μm) was provided by Hebei Lebo Metal Material Technology Co., Ltd.; and fumed silica (FS, A200) was provided by Evonik Industries AG, Germany.

2.2 Sample preparation

The preparation of EP-based absorbing inks was started with 30 g of EP resin. HAA 1021 (7.5 g) was then added to the resin and mixed at 1000 RPM in a planetary centrifugal mixer (RYX-460, Shenzhen Baoan District Ruiyue Electronic Tools and Equipment Firm) for 10 min. Subsequently, CIP was added at a specified mass fraction, and the ink was mixed for 5 min at 500 RPM, and then for 30 min at 1000 RPM. Lastly, CB was added at a specified mass fraction and mixed for 1.5 hours at 1000 RPM.

The preparation of UP-based absorbing inks was started with was started with 30 g of UP resin. MEKP (1 g) was then added, and mixed at 800 RPM in a planetary centrifugal mixer for 5 min. CIP was added at a specified mass fraction, and the ink was mixed for 5 min at 500 RPM, and then for 30 min at 800 RPM. Subsequently, 2 g of FS was added, followed by mixing at 800 RPM for 10 min. Lastly, CB was added at a specified mass fraction and mixed for 2 h at 800 RPM.

The prepared inks were loaded into a 30 CC, luer-lock syringe using a vacuum pump. It was then placed in a centrifugal defoaming machine (TP-5, Zhengzhou Beihong Machinery Equipment Co., Ltd.) and centrifuged at 5000 RPM for 5 min to remove the bubbles, following which, extrusion and printing processes can be performed.

Samples for the electromagnetic parameter test were prepared by extrusion processes. The syringe was connected to a dispensing controller (JM-8000, Taicang LiuHeJinMao Plastic Factory) using a high-pressure adapter (Suzhou Haorun Fluid Technology Co., Ltd.). The prepared ink was extruded and filled into a tube silicone mold (3.04 mm inner-diameter; 7.0 mm outer-diameter; 2.1 mm height) through manual control. It was cured for 10 h at 90 °C in an oven and placed in a dry environment at room temperature for seven days.

The microwave absorber was prepared by direct ink writing. The syringe was connected to the dispensing controller using a high-pressure adapter and a precision pressure-regulating valve (IR2000-02-A, Wuxi Zhiding Equipment Co., Ltd.). The 3D printer employed a self-assembled ink deposition system. The 180 mm×180 mm model was sliced using the Ultimaker Cura software. The printed samples were cured in an oven for 10 h at 90 °C and placed in a dry environment at room temperature for seven days.

2.3 Characterization

The transmission line coaxial method was employed to measure the complex permittivity ($\varepsilon_r = \varepsilon' - j\varepsilon''$) and complex permeability ($\mu_r = \mu' - j\mu''$) of the composites within the frequency range of 2 GHz–18 GHz using an Agilent E5071C Keysight Vector Network Analyzer (VNA) at room temperature.

The microwave absorbing performance of the printed sample was tested using a self-assembly system comprising an R&S ZNB20 vector network analyzer,

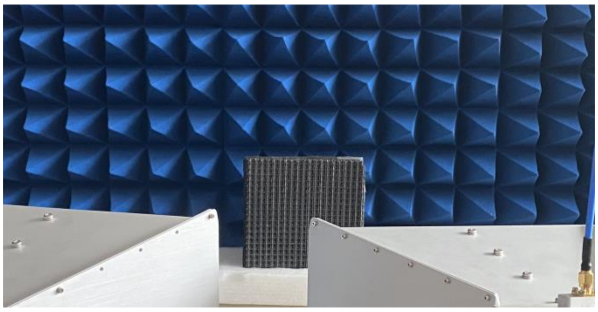

Figure 1. Measurement setup

wedge-tapered absorber, and two horn antennas, as shown in **Figure 1**. A copper foil with a thickness of approximately 0.2 mm was attached to the backside of the sample as a metal plate. A wedge-tapered absorber was installed on the back of the sample to prevent other waves being incident on the sample. Microwaves were transmitted and received by two horn antennas, which were positioned 1 m away from the sample absorber to satisfy the far-field condition. The microwave absorptivity was measured by comparing the signals reflected from the fabricated absorber with those reflected from a copper plate of the same size as the sample.

Micromorphological observation and analysis of the composites were performed using a tungsten filament scanning electron microscope (SEM, JEOL JSM-IT500LA; Japan).

3. Results and discussion

3.1 Electromagnetic Property Analyses

The excessive addition of CIP or CB causes severe agglomeration, partial uneven dispersion, and poor fluidity of the ink system. Consequently, the system cannot be extruded or printed even with the addition of a diluent. Based on our previous experimental study, the amount of magnetic loss absorber CIP added was determined to be within the range of 0-300 % of the resin mass, divided into seven groups with an increase of 50 % in each group. The dielectric loss absorber CB lies within the range of 0-10 % of the resin mass and is divided into six groups with an increase of 2 % in each group. In this study, "CB4CIP250" indicates that the additive amount of CB is 4 % of the resin mass, and the additive amount of CIP is 250 % of the resin mass. The electromagnetic parameters of all the combinations of composites with different absorbing fillers were tested. The pure CB/EP and pure CIP/EP groups were analyzed to observe the changes in the electromagnetic parameters when they were used individually. Seven groups of different CIP amounts with 4 % CB and six groups of different CB amounts with 250 % CIP were selected for analysis to determine the mutual influence and synergistic effect that exists between the two fillers.

3.1.1 Electromagnetic properties of carbon black

Pure CB/EP composites are non-magnetic materials with a complex permeability ($\mu_r = \mu' - j\mu''$) , $\mu' = 1$ and $\mu'' = 0$ by default. Therefore, only the complex permittivity of the samples was analyzed. Both the real and imaginary parts of the composite complex

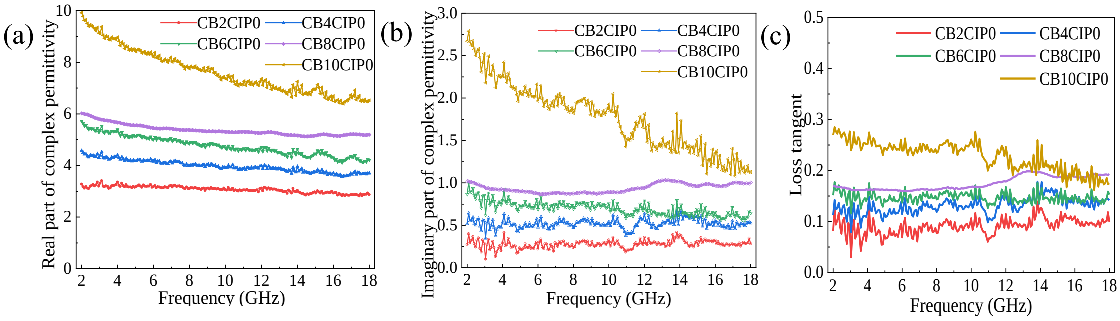

Figure 2. (a) Real part of complex permittivity (b) Imaginary part of complex permittivity (c) dielectric loss tangent of CB/EP composites

permittivity increased slightly with an increase in the CB content of up to 8 %, as shown in **Figure 2a and b**. When the CB content increased to 10 %, both the real and imaginary parts increased significantly and decreased with an increase in the frequency, i.e., with a dispersion effect.

The dielectric loss tangent of the pure CB/EP composites was calculated by $tan\,\delta_\varepsilon = \frac{\varepsilon''}{\varepsilon'}$, as shown in **Figure 2c**. A slight improvement was observed in the dielectric loss when CB below 8 % was added. It is difficult to form a continuous conductive network since the CB content is relatively low when compared to that of the matrix resin. When the CB content was increased to 10 %, the value increased by 0.2-0.3, but the dielectric loss was still weak. Essentially, the dielectric loss of the pure CB used in this study is poor and requires a large amount of addition (more than 10 %) to achieve better electromagnetic loss properties when used individually, but this causes an increase in the ink viscosity and results in the inability to print.

3.1.2 Electromagnetic properties of carbonyl iron

The pure CIP/EP composites are magnetic materials, and both the complex permittivity and complex permeability must be analyzed. The real part of the complex permittivity increased with an increase in the CIP content, while the imaginary part of the complex permittivity remained almost unchanged, as shown in **Figure 3a and b**. Therefore, the dielectric loss tangent gradually decreased with an increase in the CIP content, and its value was extremely small. They cannot form a continuous conductive network inside the resin using the additive amount considered in this study due to the large diameter of the CIP particles; consequently, only a small dielectric loss is generated on the CIP particle surface.

There was a slight increase in both the real and imaginary parts of the complex magnetic permeability with an increase in the CIP content, as shown in **Figure 3c & d**. The

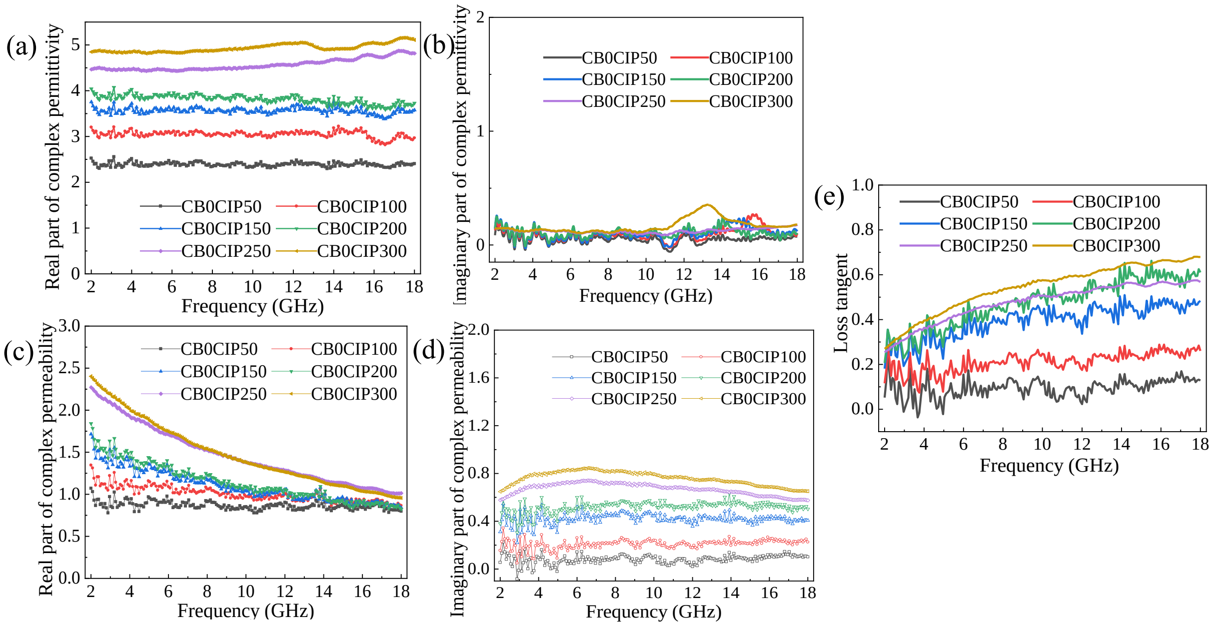

Figure 3. (a) Real part of complex permittivity (b) Imaginary part of complex permittivity (c) Real part of complex permeability (d) Imaginary part of complex permeability (e) magnetic loss tangent of CIP/EP composites

magnetic loss tangent of the pure CIP/EP composites was calculated by $tan\ \delta_{\mu} = \frac{\mu"}{\mu'}$, as shown in **Figure 3e**. The use of CIP considerably enhances the magnetic loss of the composites, but it reaches a bottleneck when the additive amount exceeds 200 %, and further improvement becomes difficult. Therefore, the magnetic loss is limited to less than 0.6 when used individually.

Generally, the magnetic loss factors of CIP include: magnetization vector rotation, hysteresis loss, magnetic domain wall resonance, natural resonance and eddy current loss. Among them, natural resonance and eddy current loss are two major contributing factors for magnetic loss of microwave absorption [31]. The eddy current

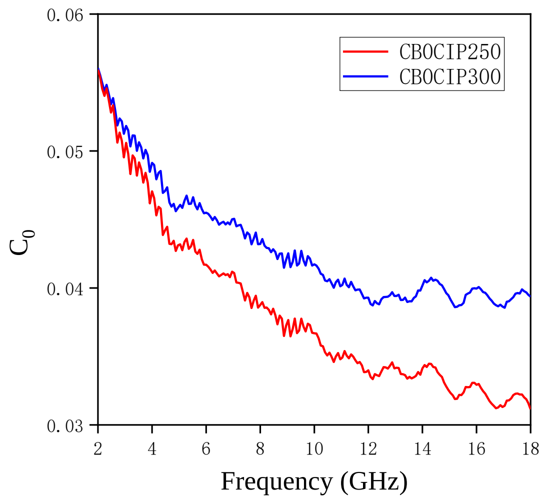

Figure 4. Values of C_0 for the CIP

loss is related to the diameter of metal particles d and the electric conductivity σ, and the relation can be approximately expressed by $\mu_r'' \approx 2\pi\mu_0(\mu_r')^2\sigma d^2 f/3$. If the magnetic loss only results from eddy current loss, the values of $C_0 = \mu''(\mu')^{-2}f^{-1}$ should be constant at the whole frequency range. [32] **Figure 4** showed that the calculated values of C_0 of the CB0CIP250 and CB0CIP300 composites decrease significantly with an increase in the frequency. Therefore, the magnetic loss of CIP is primarily attributed to natural resonance rather than to eddy current loss.

3.1.3 Electromagnetic parameters of carbon black/carbonyl iron composites

The addition of CIP was fixed at 250 %, and the effect of CB with different additions on the composite electromagnetic parameters was analyzed. A slight increase was observed in both the real and imaginary parts of the complex permittivity with an increase in the CB content, as shown in **Figure 5a and b**. Several ripples are observed for the composite with a CB content of 10 % since the resonance behavior of the composite is enhanced by the large CB content and high conductivity.[25] A significant increase was observed in both the real and imaginary parts of the complex permittivity when the CB content was increased to 10 %. However, this did not significantly affect the complex permeability, as shown in **Figure 5c and d**.

The dielectric and magnetic loss tangents of the composites containing 4 %, 8 %, and 10 % CB with 250 % CIP were calculated, and the loss mechanism of CB compounded with CIP was analyzed. A lower increase was observed in the dielectric loss tangent when the CB content increased from 4% to 8%, whereas the magnetic loss tangent decreased significantly, as shown in **Figure 5e**. The magnetic loss is still dominant in the composites since it is much higher than the dielectric loss. When the CB content was increased to 10 %, the dielectric loss was significantly improved, the magnetic loss remained unchanged, the gap between them was significantly reduced, and the dielectric loss was higher than the magnetic loss at certain frequencies. Although the main loss material is CIP, the material gradually changes from magnetic loss to dielectric loss.

Figure 5 (f-i) presents the reflection losses of the composites. The EAB was narrow when 250 % CIP was used individually, and the value of the absorption peak was small. The loss ability of the composite is enhanced with an increase in CB due to the increase in the imaginary part of the complex permittivity and complex permeability. Subsequently, the absorption peak shifts to a lower frequency and the maximum value increases significantly. However, when the CB content reached 10 %, the maximum absorption peak decreased and the EAB became narrower. This is attributed to the fact that the complex permittivity increased significantly, while the complex permeability remained almost unchanged, resulting in an impedance mismatch. Furthermore, the

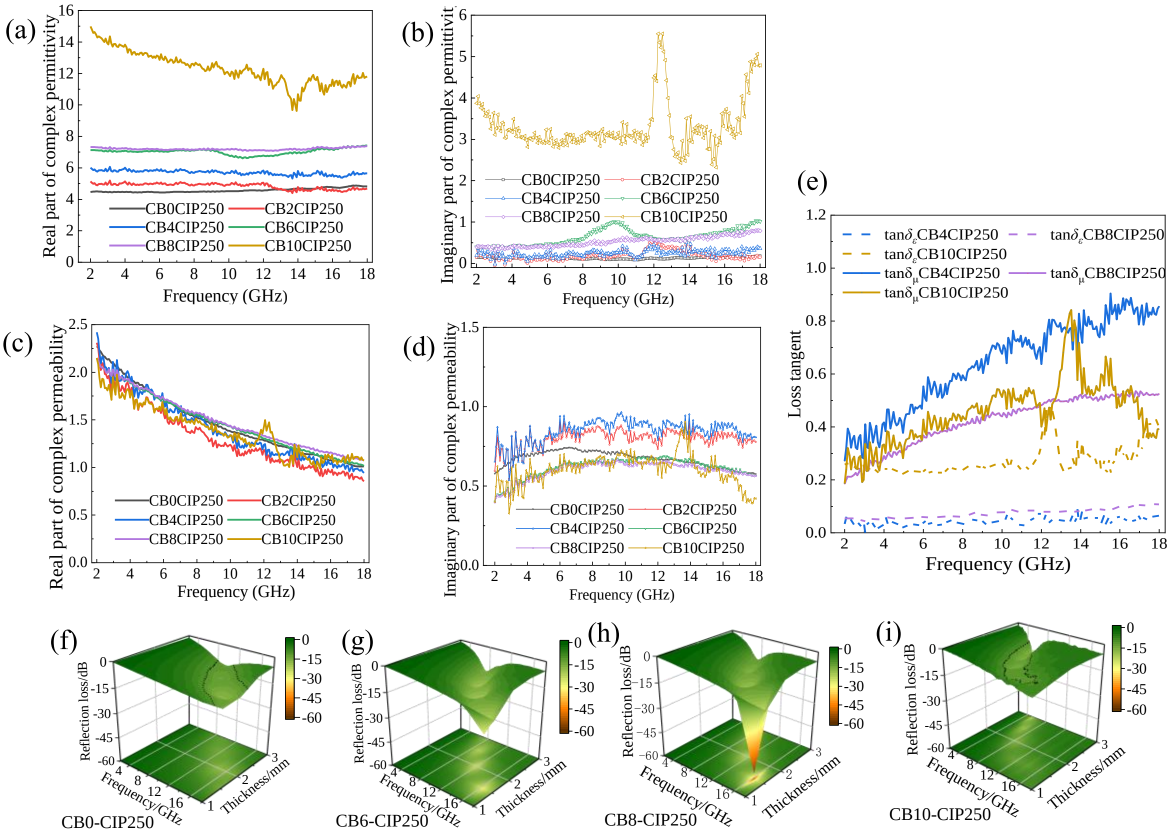

Figure 5. (a) Real part of complex permittivity (b) Imaginary part of complex permittivity (c) Real part of complex permeability (d) Imaginary part of complex permeability (e) Loss tangent (f-i) Reflection loss of CB/CIP composites

250 microwave absorption cannot be enhanced by continuously adding CB.

The addition of CB was fixed at 4 %, and the effect of CIP with different additions on the electromagnetic parameters of the composite was analyzed. There was no significant change in the imaginary part of the complex permittivity with the increase

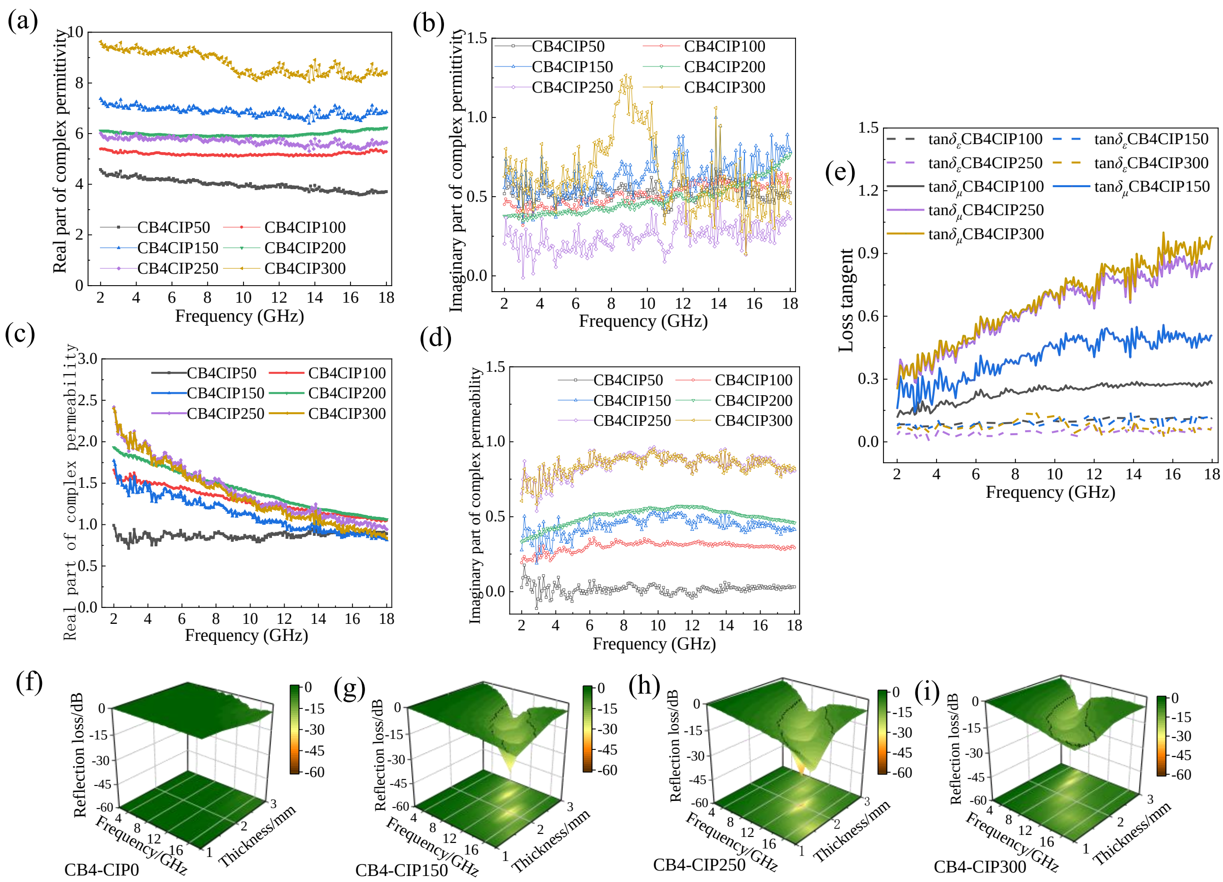

Figure 6. (a) Real part of complex permittivity (b) Imaginary part of complex permittivity (c) Real part of complex permeability (d) Imaginary part of complex permeability (e) loss tangent (f-i) Reflection loss of CB/CIP composites

in the CIP content, and the real part increases first, peaking at 150 %, decreases slightly to 250 %, and then increases significantly to 300 %, as shown in **Figure 6a and b**. Contrary to using CIP individually, after compounding CB, the influence of CIP on the dielectric properties was more complicated, and the trend weakened and then increased. It is assumed that a large amount of CIP can form a composite conductive network with CB to enhance the dielectric loss properties. Based on the complex permeability depicted in **Figure 6 c & d**, it can be observed that the addition of CIP can significantly increase the complex permeability of the composites. The dielectric and magnetic loss tangents for CIP contents of 100 %, 150 %, 250 %, and 300% were calculated, as shown in **Figure 6 e**. A slight change was observed in the values of the dielectric loss tangents, while the magnetic loss tangents increase gradually, and the attenuation of the composites is dominated by magnetic loss.

Figure 6 (f-i) depicts the reflection losses of the composites. There was no EAB and the microwave absorption performance was poor. With an increase in CIP, the impedance matching increases, the absorption peak shifts to a lower frequency, and the maximum value increases gradually. When the CIP content reached 300 %, the maximum absorption peak decreased and the EAB became narrower. Therefore, when CB/CIP is compounded, the excessive addition of one of them causes an impedance mismatch, which limits the further improvement of the absorption performance. The impedance matching can be optimized using a 3D structural design to obtain a wider EAB.

The mechanism of synergistic effects of CB and CIP can be explained as follows: Firstly, the effective complementation of CB and CIP is the key factor to enhance impedance matching. Figure 7 shows that the impedance matching ratio ($\sqrt{\mu/\varepsilon}$) of the composites varies with the

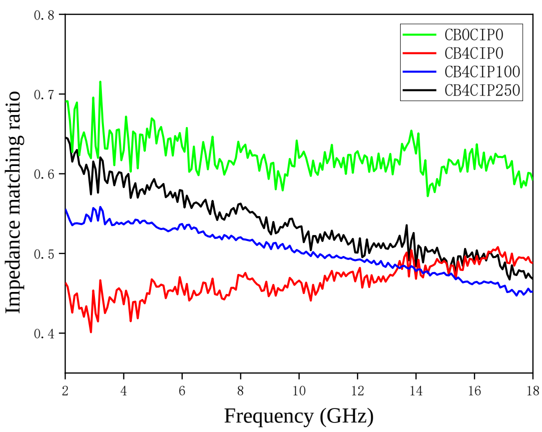

Figure 7. the impedance matching ratio of the composites

content of absorbers. It is obvious that with the increase of the CB content, the impedance matching ratio decreased, indicating that a lot of electromagnetic waves will be reflected on the surface. After compounded CIP, the impedance matching ratio increases, especially for low-frequency microwave. Secondly, the addition of CB prevents the local agglomeration of CIP. Owing to the strong activity and high surface energy of CIP, local agglomeration tends to occur during the casting or printing process after mixing, as shown in **Figure 8a**. The size of these CIP agglomeration almost exceeds 10μm. Skin depth of CIP is in the range of 1-2 μm only[33;35], which indicates that the CIP inside the agglomeration was shielded and the natural resonance of this part was weakened. So that these agglomerated CIP increases the difficulty of further increasing the magnetic loss tangent.[36;37] Meanwhile, the viscosity of the ink was increased after the addition of an appropriate amount of CB, which reduced the agglomeration of CIP after mixing. The dispersion of CIP was significantly improved, enabling further improvement of the magnetic loss tangent, as shown in **Figure 8b**. Furthermore, the addition of more CIP did not cause a reduction in the dielectric loss after mixing CB, which indicated that the synergistic effect can enhances the dielectric loss. This is because the heterogeneity of CB/CIP will make the CIP particles around CB become the center of polarization, causing the electron polarization and strong relaxation loss, and the interfacial heterogeneity among CB/CIP/EP composites can cause multiple reflections and increase the propagation routes.[38]

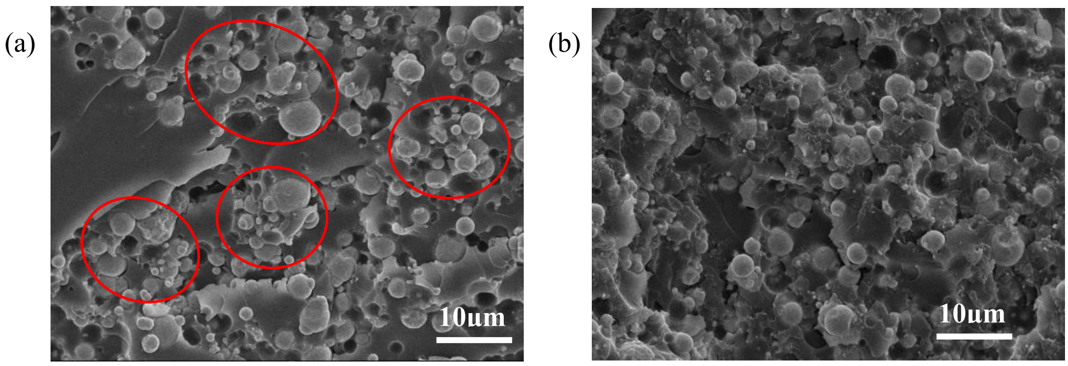

Figure 8. 2000x SEM of (a) CB0CIP250 (b) CB4CIP250. The small bright spot is CB

3.2 Design of Ultra-broadband metamaterial absorber

Based on the metamaterial equivalent medium theory, the specific electromagnetic parameter distribution can be implemented by adjusting the ratio of the background material to filling material.[39;41] For woodpile structure, the stack rod is the filling material, and the interval between them (air or other media) is the background material. Woodpile structure has the benefit of a wide range of parameter adjusting. **Figure 9** demonstrates an example of six-layer, three-material woodpile unit cell and the equivalent model. A one-layer woodpile unit cell comprised two cuboid stacked rods with the same dimension parameters placed perpendicular to each other. The main parameters included the stack rod height (*h*), period (*a*), stack rod width (*w*), and offset length from the center of the stack corresponding to the center of the unit cell (*l*). In order to simplify the parameters, the stack rod heights of the same materials are equal by default in this study. The woodpile

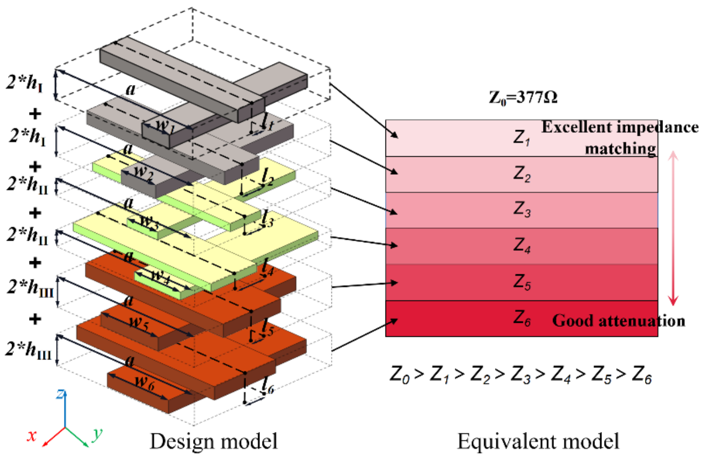

Figure 9. Design model and equivalent model of the woodpile

metamaterials are effective since the volume fraction (*fc*) of the structure can be controlled by changing the values of *w* and *a* (*fc*=*w*/*a*) to achieve different equivalent electromagnetic parameters. The effective permittivity, ε_{eff}, and effective permeability, μ_{eff}, of the composites were calculated by $\varepsilon_{eff} = \varepsilon_c f_c + (1 - f_c)\varepsilon_0$ and $\mu_{eff} = \mu_c f_c + (1 - f_c)\mu_0$, where $\varepsilon_c, \varepsilon_0, \mu_c$ and μ_0 represent the relative complex permittivity and relative complex permeability of the composites and air, respectively. Subsequently, the equivalent characteristic impedance, *Zi*, of the woodpile with different *fc* values can be calculated using equations (1):

$$Z_i = Z_0 \times \left| \sqrt{\frac{\mu_{eff}' - \mu_{eff}''}{\varepsilon_{eff}' - \varepsilon_{eff}''}} \right| \quad (1)$$

where Z_0 represents the impedance of air, whose value is 377 Ω. A GRIN absorber can be formed by arranging in the order of increasing *Zi* from the bottom (near the metal backing) to the top (near the air). The upper layer of the woodpile has excellent impedance matching performance, significantly reducing the microwave reflection. The attenuation performance of the lower woodpile layer is better, and the incident microwave can be effectively attenuated. In addition, when woodpile is applied in photonic crystals, the lower symmetry is conducive to a higher band gap ratio.[42] Therefore, this paper will also explore the possibility of widening the EAB by optimizing the symmetry of woodpile absorber through the parameter *l*. In the next section, a GRIN woodpile metamaterial with good impedance matching was designed and printed using the composite inks prepared above to achieve ultra-broadband absorption.

3.2.1 Selection of ink formulations

Based on a previous experimental study conducted on the printability of inks, the electromagnetic parameters of 42 groups of composite inks with different formulations were tested. The formulation must be screened out with a better synergistic effect of the

$$A = \left(\frac{\sqrt{2}\pi f}{c}\right) \times \sqrt{(\mu''\varepsilon'' - \mu'\varepsilon') + \sqrt{(\mu''\varepsilon'' - \mu'\varepsilon')^2 + (\mu''\varepsilon' - \mu'\varepsilon'')^2}} \quad (2)$$

two-loss absorbing fillers for the design and printing of the woodpiles. The attenuation constants of the two filler formulations were calculated according to equation (2): where f represents the microwave frequency (2 GHz-18 GHz), c denotes the light velocity in free space; and $\varepsilon', \varepsilon'', \mu'$ and μ'' represent the real and imaginary parts of the complex permittivity and complex permeability obtained from the above test. The results are presented in Table 1.

Table 1. Filler formulations and their attenuation constants

	CB0	CB2	CB4	CB6	CB8	CB10
CIP0	0.0093	0.0227	0.0298	0.0418	0.0531	0.0762
CIP50	0.0183	0.0454	0.0622	0.0567	0.0701	0.0711
CIP100	0.04612	0.0663	0.0934	0.0793	0.0971	0.0803
CIP150	0.0878	0.1012	0.1464	0.1048	0.1131	0.1632
CIP200	0.1097	0.1329	0.1403	0.1539	0.1567	0.2592
CIP250	0.1338	0.1759	0.1970	0.1821	0.1725	0.3093
CIP300	0.1581	0.1634	0.2564	0.2749	0.1907	0.3012

A comparison of the data in **Table 1** indicates that when the same amount of CIP was added, the formulations reached the attenuation constant peak with the increase in the CB amount, which is represented in green. Therefore, these three formulations with evident synergistic effects were selected as alternative materials for the design of the woodpiles. The red-marked filler formulation CB10CIP250 exhibited the strongest attenuation; therefore, it was selected as the substrate floor material for the woodpile.

3.2.2 Design of woodpile geometric parameters

The preset woodpile, *fc*, contains seven values from 0.125 to 0.875 with steps of 0.125. The equivalent characteristic impedance, *Zi*, and equivalent attenuation constant, *A*, of the woodpile with different *fc* values were calculated using equations (1) and (2), respectively. The results are presented in **Figure 10**, where the y-axis impedance matching data were divided into six levels from 150 Ω to 325 Ω. At each *Zi* level, one material and its *fc* with a lower density and better equivalent attenuation constant were selected and marked with a green arrow. These six constants, along with the substrates, are arranged in the order of increasing *Zi* from the bottom (near the metal backing) to the top (near the air) to form a gradient-index metamaterial absorber.

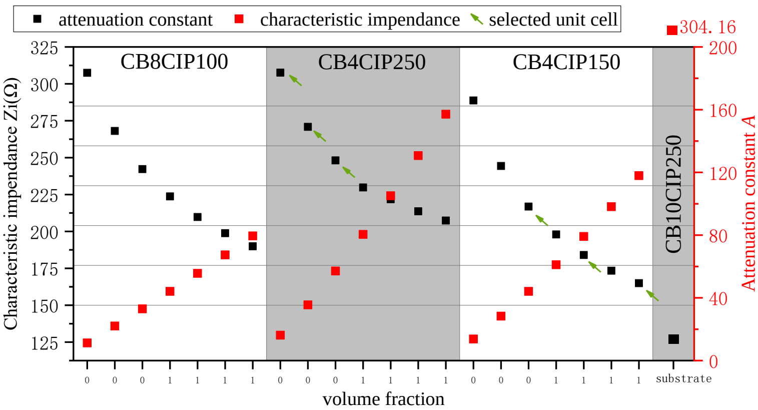

Figure 10. *Zi* and *a* of different unit cells materials and *fc*

This seven-layer woodpile with the selected materials and their *fc* values was modeled using CST software. The value of *a* was first selected from 6 mm to 11 mm based on the self-assembly 3D printer, to determine its effect on the microwave absorption. In the simulation, the height of stack rods was initially fixed at 1 mm, and the total height was 13 mm. The results are present in **Figure 11a**. The position of the absorption peak gradually shifted to a lower frequency with an increase in period, *a*, and the bandwidth increased. However, the peak value of the reflection loss first increases and then decreases; it can reach more than -40 dB when *a* is 8 or 9 mm. Therefore, in this study, the period of the woodpile was considered as 9 mm, which presents a wider bandwidth and better reflection loss.

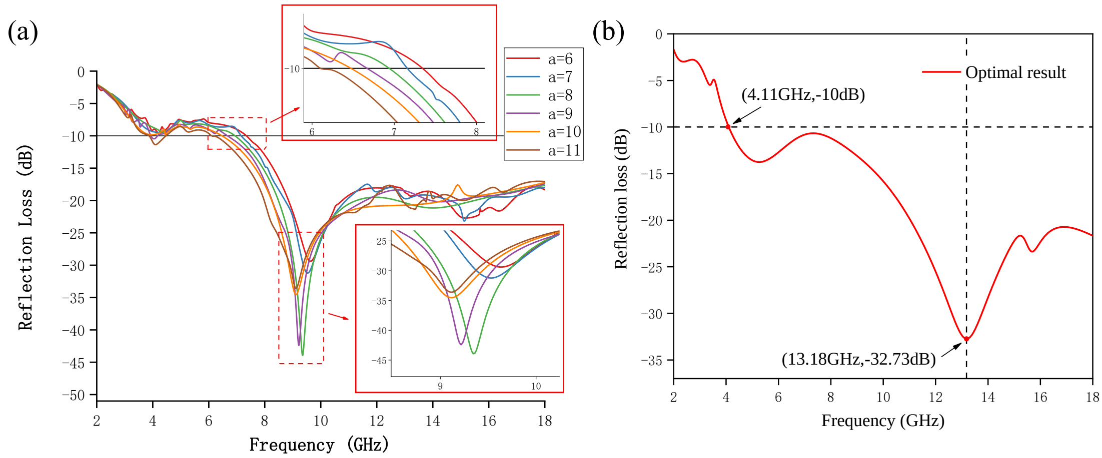

Figure 11. (a) RL of Influence different period; (b) RL for optimal woodpile structural parameters

Subsequently, the stack rods composed of the same formulation were set to the same height, *h*. The *h* values of the stack rods printed using CB4CIP250, CB4CIP150, and CB10CIP250 correspond to *hp*, *hs*, and *hj*, respectively. The better *h* value of each layer was determined using the multi parameter sweep of the CST software. The *hj* values were 0.5 mm, 1 mm, 1.5 mm, and 2 mm, and *hp* and *hs* were 0.5 mm, 0.6 mm, 0.8 mm, and 1 mm, respectively. Considering moderate height and wide bandwidth, by comparing the 64 sets of the calculation results, *hp*, *hs*, and *hj* were set to 0.6 mm, 0.5 mm, and 2 mm, respectively. When the total height of the woodpile was 8.6 mm, the reflection loss reaches -32.73 dB with a bandwidth of 13.89 GHz, as shown in **Figure 11b**. The height was reduced when compared to that in **Figure 11a**; consequently, the absorption peak shifted to a higher frequency.

3.2.3 Woodpile arrangement optimization

The woodpile designed using the proposed method presents a wider bandwidth below 18 GHz and stronger reflection loss at a lower cost when compared to the woodpile absorber fabricated using graphene/PLA composite filaments and FDM 3D printing.[24] However, the bandwidth does not completely encompass the C, X, and Ku bands. Therefore, we have also explored the possibility of optimizing the woodpile arrangement to widen the bandwidth. The above design and other woodpile absorbers typically adopt a simple tetragonal (ST) arrangement[24, 43], that is, l=0 for all the stack rods in the structure. Different geometric symmetries can be achieved by using different values of l. For example, when $l=a/4$ for all the stack rods and the offset directions of the two adjacent stack rods are opposite, the woodpile is a body-centered cubic (BCC) configure, and when the l of each stack rod is irregular, it is an asymmetric woodpile.

The better asymmetric woodpile offset length of each layer was determined based on the multi parameter sweep of the CST software. The values of each layer (l_n) were taken from 2.25, 1.125, 0, -1.125, and -2.25, that is, $a/4$, $a/8$, 0, -$a/8$, and -$a/4$. When compared to the simulation results, it was observed that the bandwidth of the asymmetric woodpile was the widest when $l1$ to $l6$ were taken as 2.25, -2.25, 2.25, -2.25, 1.125, and -1.125, respectively. Hereafter, the woodpile with these offset lengths is called an asymmetric woodpile. **Figure 12a** presents the microwave absorption comparison of the asymmetric woodpile, BCC woodpile, and ST woodpile. The EAB is slightly improved when the symmetry of the woodpile is reduced without changing the original equivalent impedance matching gradient. The bandwidth was increased from 13.89 GHz to 14.1 GHz, and completely encompasses the C, X, and Ku bands. **Figure 12b** depicts the final design of the woodpile unit.

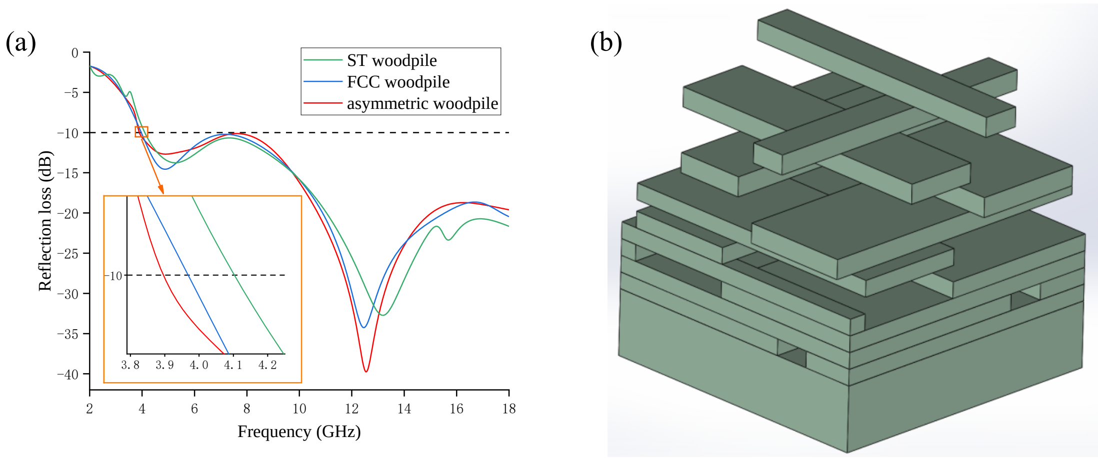

Figure 12. (a) RL of woodpiles with different symmetry (b) Asymmetric woodpile unit cell

The angular performance of the asymmetric woodpile was simulated using CST software, and its absorption spectrum with incident angles from 0 ° to 70 ° under transverse electric (TE) and transverse magnetic (TM) polarization are depicted in

Figure 13. The bandwidth gradually decreased with the increase in the incident angle, and the strongest reflection loss occurred at a small angle (10 °-30 °) instead of at 0 °. This is attributed to the fact that when microwaves are incident at a small angle, they can enter the internal gap of the woodpile more easily and reflect multiple times between the stack rods. Multiple scattering effects are produced on the edge, which increases the propagation distance of the microwaves in the structure and enhances the microwave loss.[44;45] Typically, the absorption of TM waves is more stable than that of TE waves. The EAB of TE and TM waves can reach up to 10.34 GHz and 12.87 GHz at an incident angle of 50 °. Therefore, the designed woodpile exhibited an excellent angular performance.

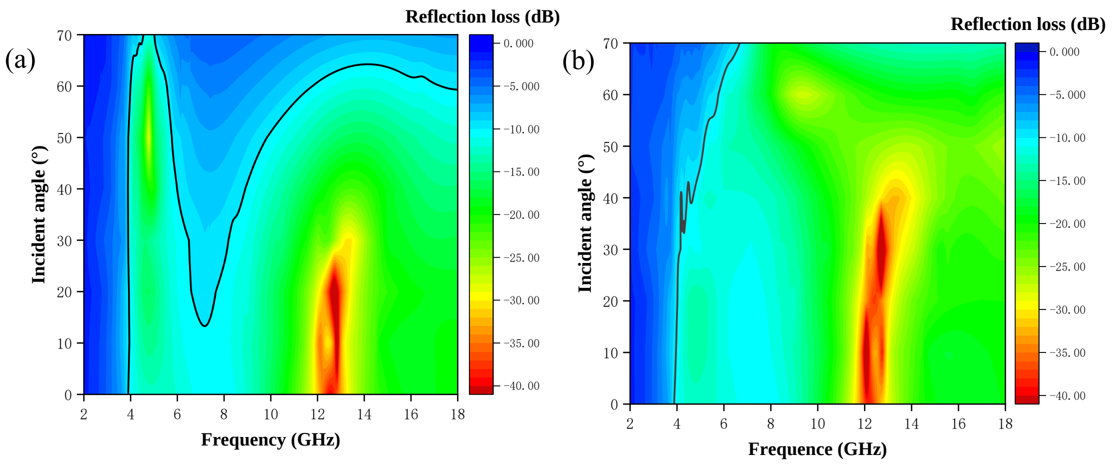

Figure 13. Absorption contour with the variation of incident angles (0°-70°) at: (a) TE polarization; (b) TM polarization. The black line represents the bandwidth boundary of -10dB.

3.3 Absorption mechanism

From the above results, it was observed that different woodpile arrangements affect the bandwidth of a structure with the same impedance gradient and attenuation constant. The -10 dB absorption bandwidth widening of the asymmetric woodpile metamaterial corresponding to the ST woodpile metamaterial was primarily observed at the lowest frequency, i.e., at 3.9 GHz. Therefore, the power loss distribution at this frequency was monitored using CST software to better understand the mechanism behind the bandwidth widening. Firstly, the power loss distribution of the ST woodpile is uneven, and the positions with strong loss are primarily concentrated in the area with denser woodpiles placed above, as marked by the black wireframe in **Figure 14 b and c**. As a comparison, the power loss of the asymmetric woodpile floor is relatively even, as shown in **Figure 14 e and f**. Secondly, the power loss at the positions marked by the red circle on the ST woodpile is lower than that of the asymmetric woodpile, as shown

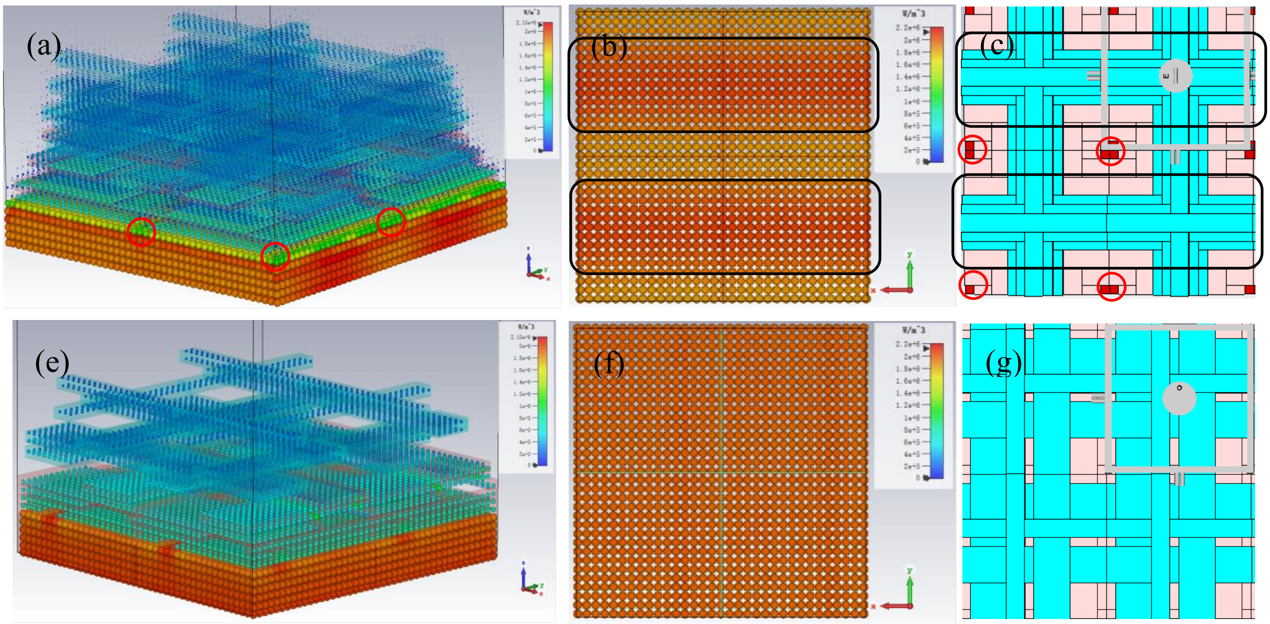

Figure 14. (a) Isometric drawing view and (b) Bottom view of ST woodpile power loss distribution; (c) Top view of symmetrical woodpile structure; (e) Isometric drawing view and (f) Bottom view of asymmetric woodpile power loss distribution; (d) Top view of asymmetric woodpile structure.

in **Figure 14 a and c**. This position corresponds to the woodpile substrate that is directly exposed to the microwave incident port, as shown in Figure 11c. Considering these two phenomena together, it is assumed that the ST woodpile has a local impedance mismatch, which results in the bandwidth narrowing.

Additionally, the difference in the impedance matching between two woodpile arrangements can be determined by calculating the effective input impedance (Zeff) using formula 3 as follows:

$$Z_{eff} = \sqrt{\frac{(1+S_{11})^2 - {S_{21}}^2}{(1-S_{11})^2 - {S_{21}}^2}} \tag{3}$$

Since the structure was backed by copper foil, |S21|=0. The Zeff was calculated using the S11-parameters in Figure 12a and simulated by the CST software. The Zeff variation trend of the two woodpiles is consistent, *with a* high fluctuation from 2 GHz to 3.9 GHz, and an impedance mismatch results in poor absorption in this frequency range, as shown in **Figure 15**. The real and imaginary parts of Zeff gradually approached 1 and 0, respectively, from 3.9 GHz to high frequency, indicating good impedance matching with the air of the woodpile. Particularly, the real and imaginary parts of the asymmetric woodpile were closer to 1 and 0 than the ST woodpile at the frequency of 3.9 GHz, indicating that the asymmetric arrangement improves the

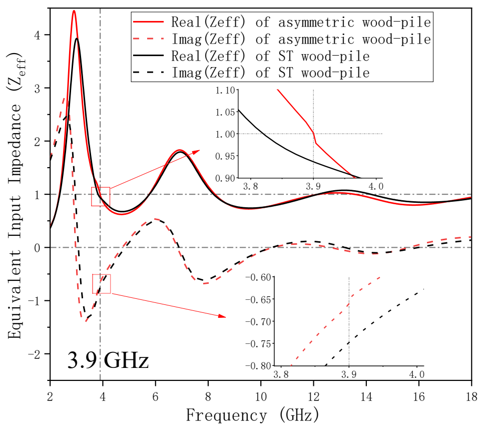

Figure 15. Calculated effective impedance of the two woodpiles

impedance matching of the woodpile, due to which the absorption bandwidth can be slightly widened.

To better understand the working mechanism behind the designed woodpile metamaterial absorber, we monitored its electric field, magnetic field, and power loss distribution at two absorption peak frequencies of the RL curve shown in Figure 9a, i.e., 5.2 GHz and 12.8 GHz. Each distribution presents a perspective view of the xo-z plane. It can be clearly observed that there is a spatial separation between the electric and magnetic fields at a frequency of 5.2 GHz, and that standing waves are generated inside the woodpile, with a typical λ/4 resonance, as shown in **Figure 16a**.[46]

Additionally, the power loss primarily occurs in the substrate layer, and the magnetic field also reaches its maximum. The magnetic field induces a high magnetic loss of the CIP filler. A power loss of 12.8 GHz primarily occurs in the first three layers of the woodpile, as shown in **Figure 16b**. The electric field reaches its maximum and the magnetic field is generally focused, exhibiting a strong synergistic effect between the two loss fillers.

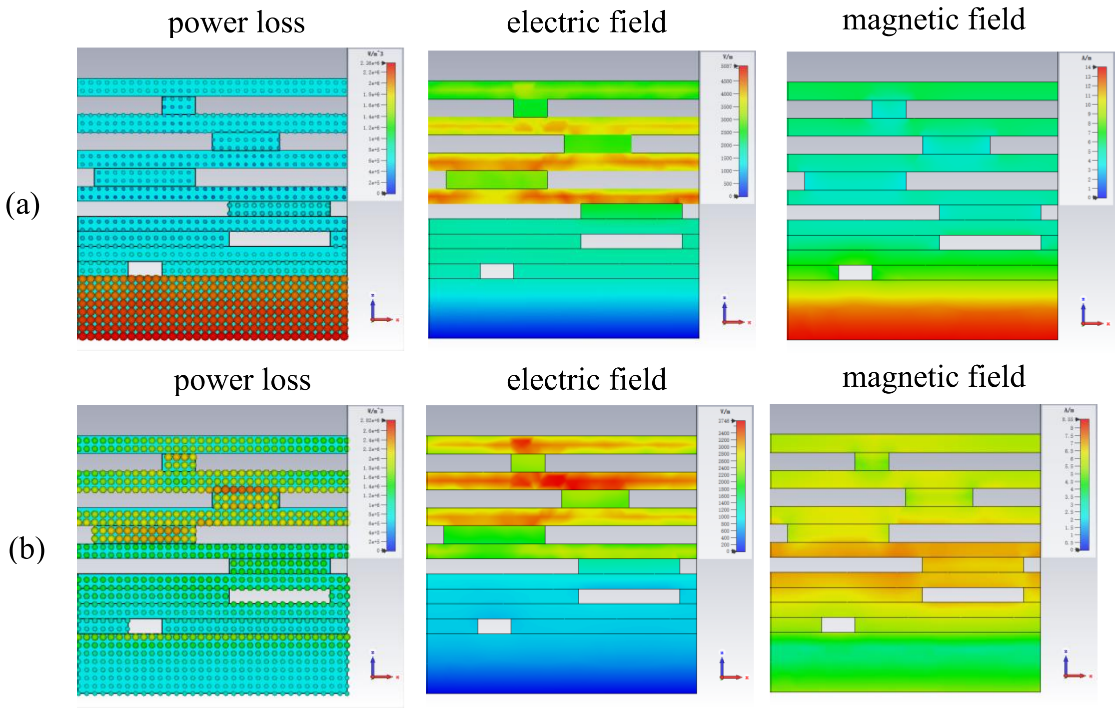

Figure 16. The distributions of power loss, magnetic field, and electric field under normal incidence at (a) 5.2 GHz and (b) 12.8 GHz.

3.4 Fabrication and measurement

The designed asymmetric woodpile was fabricated using direct-ink-writing 3D printing to verify the accuracy and reliability of our simulation results, as shown in **Figure 17a**. **Figure 17b** depicts the measured and simulated curves. Overall, the trend of the measured curve is consistent with that of the simulation, demonstrating the accuracy of

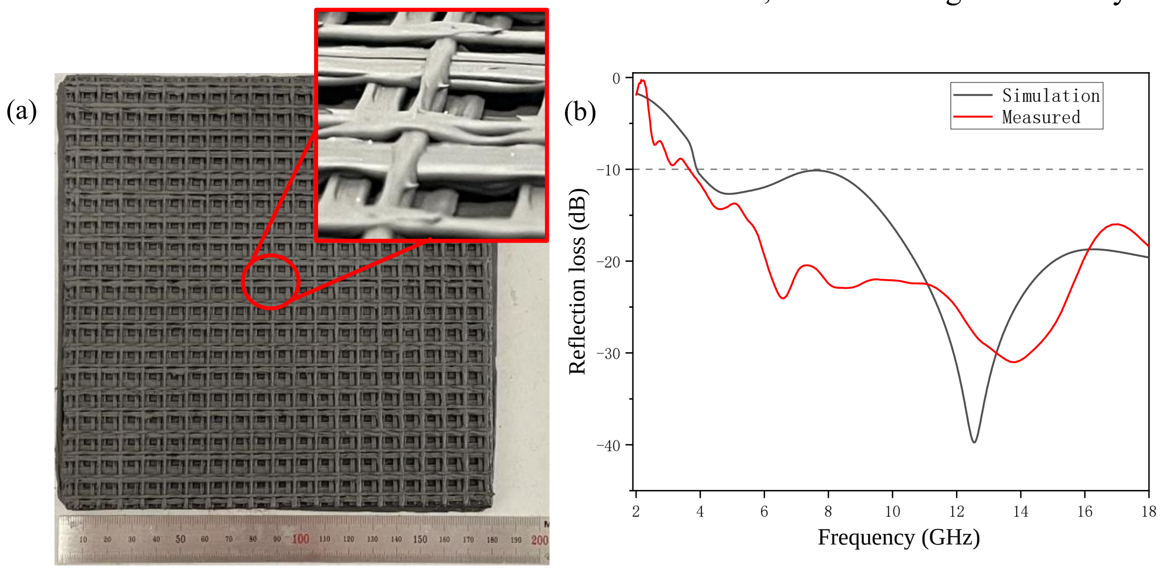

Figure 17. (a) Photograph of 3D printing sample and local details; (b) Simulated and measured RL of proposed woodpile

the simulation. The measured EAB ranges from 3.7 GHz to 18 GHz, which is slightly wider than that of the simulation. However, at a frequency of 4 GHz-10 GHz, the measured reflection loss was greater than the simulated value. This can be attributed to the slight collapse of the suspended materials during direct ink writing. The material closer to the top layer has a longer suspended length, causing the materials at the top to collapse into the middle of the structure. This corresponds to the main absorption area of 4 GHz-10 GHz, and more absorbing materials produce greater reflection loss values. This also accounts for the fact that the measured absorption peak was smaller than the simulated peak. The means of improving shape retention by applying additional energy during DIW printing, such as microwave or ultraviolet radiation, for the fabrication of a woodpile structure with more precise geometric details will be addressed in future works.

4.Conclusions

In this study, CB/CIP composite inks were prepared, and they demonstrated an evident synergistic effect. The addition of CB resulted in a corresponding increase in the viscosity of the inks and reduction of the agglomeration of CIP. The full effect of the natural resonance enhanced the magnetic loss of the composite inks. Additionally, a new interface polarization between the CB and CIP enhanced the dielectric loss of the composite inks. Excellent impedance matching characteristics were achieved using the designed asymmetric woodpile metamaterial fabricated through DIW 3D printing. The cost required to satisfy the -10 dB reflectivity bandwidth in the frequency range of 3.9 GHz to 18 GHz with a thickness of 8.6 mm, and to encompass the entire C, X, and Ku bands is low. Furthermore, the absorption bandwidth can reach more than 10 GHz with incident angles from 0 ° to 50 ° for TE or TM polarization. The proposed inks and the designed asymmetric woodpiles present considerable application potential in high-performance microwave absorbers.

Acknowledgements

This work was supported by National Natural Science Foundation of China [51475174] and FuJian Provincial Science and Technology Plan Pilot Project (Grant No.2019H0014).

References

[1] C. M. Watts, X. Liu, W. J. Padilla, *ADV. MATER.* **2012**, 24, ‘DOI:‘ 10.1002/adma.201200674P98.

[2] D. Min, W. Zhou, Y. Qing, F. Luo, D. Zhu, *NANO* **2017**, 12, ‘DOI:‘ 10.1142/S17932920175008981750089.

[3] A. N. Yusoff, M. H. Abdullah, S. H. Ahmad, S. F. Jusoh, A. A. Mansor, S. A. A. Hamid, *J. APPL. PHYS.* **2002**, 92, ‘DOI:‘ 10.1063/1.1489092876.

[4] K. Chen, X. Luo, G. Ding, J. Zhao, Y. Feng, T. Jiang, *EPJ Applied Metamaterials* **2019**, 6, ‘DOI:‘ 10.1051/epjam/20180111.

[5] Y. C. Qing, W. C. Zhou, S. Jia, F. Luo, D. M. Zhu, *Applied Physics A* **2010**, 100, ‘DOI:‘ 10.1007/s00339-010-5738-51177.

[6] L. Liu, Y. Duan, L. Ma, S. Liu, Z. Yu, *APPL. SURF. SCI.* **2010**, 257, ‘DOI:‘ 10.1016/j.apsusc.2010.07.078842.

[7] X. Sun, J. He, G. Li, J. Tang, T. Wang, Y. Guo, H. Xue, *J. MATER CHEM C.* **2013**, 1, ‘DOI:‘ 10.1039/C2TC00159D765.

[8] K. Li, R. Zhao, J. Xia, G. Zhao, *ADV. ENG. MATER.* **2020**, 22, ‘DOI:‘ 10.1002/adem.2019007801900780.

[9] W. Zhou, L. Long, G. Bu, Y. Li, ADV. ENG. MATER. 2019, 21, ‘DOI: ‘ 10.1002/adem.2018006651800665.

[10] L. Yin, J. Doyhamboure--Fouquet, X. Tian, D. Li, *Composites Part B: Engineering* **2018**, 132, ‘DOI:‘ 10.1016/j.compositesb.2017.09.003178.

[11] Y. Yang, W. Zhao, Z. Wu, J. Zhao, T. Jiang, K. Chen, Y. Feng, MICROW. OPT. TECHN. LET. 2022, 64, ‘DOI:‘ 10.1002/mop.33151500.

[12] N. H. Faisal, R. Ahmed, N. Sellami, A. Prathuru, J. Njuguna, F. Venturi, T. Hussain, H. Y. Nezhad, N. K. Katiyar, S. Goel, H. Upadhyaya, S. Joshi, F. Muhammad-Sukki, R. Prabhu, T. Mallick, W. Whittow, S. Kamnis, ADV. ENG. MATER. 2022, 24, ‘DOI:‘ 10.1002/adem.2022001712200171.

[13] H. Zhuang, X. Wang, J. Wang, M. Guo, D. Tang, B. Zhang, X. Chen, P. Chen, Y. Yang, *Journal of Physics D: Applied Physics* **2020**, 53, ‘DOI:‘ 10.1088/1361-6463/ab8138255502.

[14] Y. Pang, H. Cheng, Y. Zhou, J. Wang, *J. APPL. PHYS.* **2013**, 113, ‘DOI:‘ 10.1063/1.479363184907.

[15] X. Lleshi, R. Grelot, T. Q. Van Hoang, B. Loiseaux, D. Lippens, ‘presented at‘, 2019-01-01, **2019**.

[16] D. Zhou, X. Huang, Z. Du, *IEEE ANTENN WIREL PR* **2017**, 16,

'DOI:' 10.1109/LAWP.2016.2560904133.

[17] H. Mei, W. Yang, X. Zhao, L. Yao, Y. Yao, C. Chen, L. Cheng, *MATER. DESIGN* **2021**, 197, 'DOI:' 10.1016/j.matdes.2020.109271109271.

[18] D. Yang, Y. Yin, Z. Zhang, D. Li, Y. Cao, *MATER. LETT.* **2020**, 281, 'DOI:' 10.1016/j.matlet.2020.128571128571.

[19] Y. Duan, Q. Liang, Z. Yang, Z. Li, H. Yin, Y. Cao, D. Li, *MATER. DESIGN* **2021**, 208, 'DOI:' 10.1016/j.matdes.2021.109900109900.

[20] W. Lai, Y. Wang, J. He, *POLYMERS-BASEL* **2020**, 12, 'DOI:' 10.3390/polym120612171217.

[21] Z. Pei, Y. Xu, F. Wei, T. Liu, D. Su, *J. MAGN. MAGN. MATER.* **2020**, 493, 'DOI:' 10.1016/j.jmmm.2019.165742165742.

[22] J. Ren, J. Y. Yin, *MATERIALS* **2018**, 11.

[23] Z. Li, D. Feng, B. Li, D. Xie, Y. Mei, T. Zeng, ADV. ENG. MATER. 2022, 24, 'DOI:' 10.1002/adem.2021013922101392.

[24] L. Yin, X. Tian, Z. Shang, D. Li, *MATER. LETT.* **2019**, 239, 'DOI:' 10.1016/j.matlet.2018.12.087132.

[25] P. Gong, Y. Li, C. Xin, Q. Chen, L. Hao, Q. Sun, Z. Li, CERAM. INT. 2022, 48, 'DOI:' 10.1016/j.ceramint.2021.12.1909873.

[26] Y. Zuo, X. Su, X. Li, Z. Yao, T. Yu, J. Zhou, J. Li, J. Lu, J. Ding, CARBON 2020, 167, 'DOI:' 10.1016/j.carbon.2020.05.07162.

[27] H. Mei, X. Zhao, S. Zhou, D. Han, S. Xiao, L. Cheng, CHEM. ENG. J. 2019, 372, 'DOI:' 10.1016/j.cej.2019.05.011940.

[28] H. Mei, W. Yang, X. Zhao, L. Yao, Y. Yao, C. Chen, L. Cheng, MATER. DESIGN 2021, 197, ‘DOI:‘ 10.1016/j.matdes.2020.109271109271.

[29] H. Huang, W. Wang, M. Hua, J. Kuang, Y. Ma, Z. Guo, W. Xie, Physica B: Condensed Matter 2020, 595, ‘DOI:‘ 10.1016/j.physb.2020.412368412368.

[30] Z. Li, Y. Li, B. Shi, D. Tang, Y. Wang, L. Hao, CERAM. INT. 2022, 48, ‘DOI:‘ 10.1016/j.ceramint.2021.12.1149277.

[31] M. Wu, Y. D. Zhang, S. Hui, T. D. Xiao, S. Ge, W. A. Hines, J. I. Budnick, M. J. Yacaman, *J. APPL. PHYS.* **2002**, 92, ‘DOI:‘ 10.1063/1.15187576809.

[32] B. Lu, X. L. Dong, H. Huang, X. F. Zhang, X. G. Zhu, J. P. Lei, J. P. Sun, *J. MAGN. MAGN. MATER.* **2008**, 320, ‘DOI:‘ 10.1016/j.jmmm.2007.10.0301106.

[33] K. S. Sista, S. Dwarapudi, D. Kumar, G. R. Sinha, A. P. Moon, *J. ALLOY. COMPD* **2021**, 853, ‘DOI:‘ 10.1016/j.jallcom.2020.157251157251.

[34] L. Z. Wu, J. Ding, H. B. Jiang, L. F. Chen, C. K. Ong, *J. MAGN. MAGN. MATER.* **2005**, 285, ‘DOI:‘ 10.1016/j.jmmm.2004.07.045233.

[35] C. Yin, Y. Cao, J. Fan, L. Bai, F. Ding, F. Yuan, *APPL. SURF. SCI.* **2013**, 270, ‘DOI:‘ 10.1016/j.apsusc.2013.01.044432.

[36] X. Li, Y. Zhang, J. Chen, Y. Duan, G. Wu, G. Ma, *MATER. TECHNOL.* **2013**, 29, ‘DOI:‘ 10.1179/1753555713Y.000000009657.

[37] S. Sugimoto, T. Maeda, D. Book, T. Kagotani, K. Inomata, M. Homma, H. Ota, Y. Houjou, R. Sato, **2002**, 330-332, 306.

[38] Y. Duan, Y. Liu, Y. Cui, G. Ma, W. Tongmin, *PROG. ORG. COAT.* **2018**, 125, ‘DOI:‘ 10.1016/j.porgcoat.2018.08.03089.

[39] E. F. Kuester, C. L. Holloway, *IEEE T. MICROW. THEORY* **1990**, 38, 1752.

[40] H. Mei, W. Yang, D. Yang, L. Yao, Y. Yao, C. Chen, L. Cheng, *Optics & Laser Technology* **2022**, 147, ‘DOI:‘ 10.1016/j.optlastec.2021.107627107627.

[41] X. Tian, L. Yin, D. Li, *Opto-Elec Eng*, 2017, 44(1): 69–76

[42] H. Liu, J. Yao, D. Xu, P. Wang, *OPT. EXPRESS* **2007**, 15, ‘DOI:‘ 10.1364/OE.15.000695695.

[43] L. Yin, X. Tian, *Journal of physics. Conference series* **2021**, 1721, ‘DOI:‘ 10.1088/1742-6596/1721/1/01202612026.

[44] H. Mei, X. Zhao, S. Zhou, D. Han, S. Xiao, L. Cheng, *CHEM. ENG. J.* **2019**, 372, ‘DOI:‘ 10.1016/j.cej.2019.05.011940.

[45] Q. Zhou, X. Yin, F. Ye, X. Liu, L. Cheng, L. Zhang, *MATER. DESIGN* **2017**, 123, ‘DOI:‘ 10.1016/j.matdes.2017.03.04446.

[46] X. Chen, Z. Wu, Z. Zhang, Y. Zou, *Optics & Laser Technology* **2020**, 124, ‘DOI:‘ 10.1016/j.optlastec.2019.105972105972.